distribution, though $\alpha = \frac{1}{4}\pi$ is desirable in that the even and odd portions of the object are given equal weight in the transform. It is sufficient for α to be near $\frac{1}{4}\pi$ for the characteristic properties of the Hartley transform to be realized.

The quarter-fringe departure of the fringe system from the origin does not require absolute determination; the precise displacement makes itself apparent as soon as the offset point source has appreciable extent, as explained next.

The transparency (Fig. 2) is a circular aperture centred at (a, b) on an opaque field. A disc of radius R located at the origin has identical Hartley and Fourier transforms proportional to jinc $2Rq$, where jinc q, the two-dimensional Fourier transform of a circular pupil of unit diameter, is given by jinc $q = J_1(\pi q)/2q$, and $q = \sqrt{u^2 + v^2}$ is the radial coordinate in the (u, v)-plane I. When the transparency is shifted from the origin to (a, b) the Fourier transform acquires a multiplicative phase factor $\exp[-i2\pi(au + bv)]$ but this shift has no effect on the Fourier magnitude, only a phase gradient being created on the (u, v)-plane; consequently a photograph taken in the Fourier transform plane (Fig. 3a) cannot distinguish between a centred disc and a displaced one. The Hartley transform in this case responds to the shift[2] by acquiring a multiplicative factor $\mathrm{cas}[2\pi(au + bv)]$, which does affect the magnitude. Figure 3b shows the Hartley intensity corresponding to the displaced disk. The jinc function factor, indicated by the concentric null rings centred on $u = 0$, $v = 0$, provides the origin indication mentioned above. In addition to the ring structure, this Hartley transform has fringes due to multiplication by a properly orientated cas function corrugation whose frequency and orientation are determined by the displacement. The function cas θ has a maximum at $\theta = \frac{1}{4}\pi$ and a null at $\theta = -\frac{1}{4}\pi$ and one can verify in Fig. 3b that the origin falls midway between a fringe null and a fringe maximum.

The eccentricity of the fringes illustrates the absence of symmetry that characterizes the Hartley transform and effectively enables the phase information to be encoded as amplitude. For the particular input chosen in Fig. 2, the observed Hartley transform (Fig. 3b) indicates the magnitude and direction of the displacement from the (x, y) origin and serves as an example of information that is preserved in the Hartley intensity but is, by contrast, lost in the Fourier intensity. The reciprocal nature of the transform is demonstrated by placing a properly adjusted mirror at I which causes the field $H(u, v)$ to act as the input into the transformer with the output (the reconstructed object) now appearing near T. A beam-splitter placed between T and L_1 can be used to verify the correctness of the reconstructed object.

In some circumstances holography permits the encoding of optical phase by the precise spatial location of interference fringes whose spacing is of the order of the optical wavelength. The cas-function fringes in Hartley phase encoding are in general coarser, and thus tolerant to deformation, being connected with the object structure rather than with the $\frac{1}{2}\lambda$ sec i characteristic of holography. Hartley holograms with both weak and strong isophase reference beams and with oblique reference beams have been produced.

Two other optical arrangements[2,4], which have not yet been implemented, one involving roof prisms and one a cube corner, offer alternative Hartley transformers that have the feature of being adaptable to incoherent illumination.

This work was supported by the Office of Naval Research and by an NSF fellowship. We thank Dr Eric Gustafson for making optical equipment available.

Received 27 July; accepted 29 September 1987.

1. Hartley, R. V. L. *Proc. Inst. Radio Engrs* **30**, 144-150 (1942).
2. Bracewell, R. N. *The Hartley Transform*, 3-112 (Oxford University Press, New York, 1986).
3. Bracewell, R. N., Buneman, O., Hao, H. & Villasenor, J. *Proc. Inst. Elect. Electron. Engrs.* **74**, 1283-1284 (1986).
4. Bracewell, R. N., Bartelt, H., Lohmann, A. W. & Streibl, N. *Appl. Opt.* **24**, 1401-1402 (1985).
5. Bracewell, R. N. *J. opt. Soc. Am.* **73**, 1832-1835 (1983).

Static compression of H_2O-ice to 128 GPa (1.28 Mbar)

R. J. Hemley*, A. P. Jephcoat*, H. K. Mao*, C. S. Zha*, L. W. Finger* & D. E. Cox†

* Geophysical Laboratory, Carnegie Institution of Washington, 2801 Upton Street NW, Washington, DC 20008, USA
† Brookhaven National Laboratory, Upton, New York 11973, USA

The high-pressure behaviour of H_2O is of fundamental importance in both condensed matter and planetary physics[1,2]. The hydrogen bonding in this system gives rise to a variety of phases at low pressures and temperatures (that is, <2 GPa and <300 K), including the recently discovered high-density amorphous phases[3]. Structural and equation-of-state[4,5] and spectroscopic[6-8] studies have been carried out in the 30–50 GPa range on the dense ices (ice VII and VIII), but no data are available on the properties of solid H_2O in the megabar pressure range (>100 GPa) where a variety of stable phases, including the metallic form, have been proposed[9]. Information on the properties of H_2O at these pressures has been limited to the results of shock-wave experiments, which probe the fluid phase at high pressures and temperatures[10], and to theoretical statistical electron calculations[11-15]. In this study we have compressed ice in a diamond-anvil cell to 128 GPa and measured the molar volume as a function of pressure by synchrotron X-ray diffraction techniques. The diffraction data are consistent with the body-centred cubic (b.c.c.) oxygen sublattice of ice VII persisting to the highest pressures of our measurements. The measured equation of state indicates that ice is less compressible at very high pressures than is suggested by recent experiments in the 30–50 GPa range, but more compressible than statistical electron and recent pair-potential models predict.

The experiments were made possible by the use of several new applications of X-ray diffraction in the megabar pressure range with the diamond-anvil high-pressure cell. The X-ray diffraction was measured by energy-dispersive scattering techniques with a polychromatic (white) synchrotron X-ray beam[16,17]. Synchrotron radiation, with its high intensity and low beam divergence, was crucial for these experiments. High X-ray intensity is necessary to obtain high-quality diffraction data because of the small X-ray scattering cross-section of H_2O, a low-Z material. More significant, particularly above ~20 GPa, is the fact that a small beam diameter must be used to minimize the effect of pressure gradients arising from the increasing yield strength of ice[4]. Measurements with a large X-ray beam at these pressures can result in both line-broadening effects and errors in the pressure determination. In the present experiments, the X-ray beam was collimated down to the 10–30 μm range[17]. Finally, to measure the pressure precisely at the sample volume probed by diffraction, the recently developed X-ray-induced ruby fluorescence method was used[18,19]. With this technique the pressure is measured from the shift of the R_1 fluorescence line from ruby chips embedded in the sample, as in the conventional ruby method[20]. In the X-ray-induced technique, however, the luminescence from the ruby is excited by the X-rays simultaneously with the diffraction measurement, instead of separately with a laser source. The fluorescence spectra obtained by the X-ray method are identical to those obtained in previous calibration studies over the pressure range of the present experiments[18-21].

Previous structural studies of ice VII have shown that this phase has a broad stability field at room temperature, extending from 2.3 GPa to at least 50 GPa[5]. The structure is characterized by a b.c.c. arrangement of oxygen ions with some degree of disorder in the protons[1]. In our experiments, doubly distilled and deionized H_2O and ruby were loaded in a high-pressure cell mounted with bevelled diamonds and designed for optical

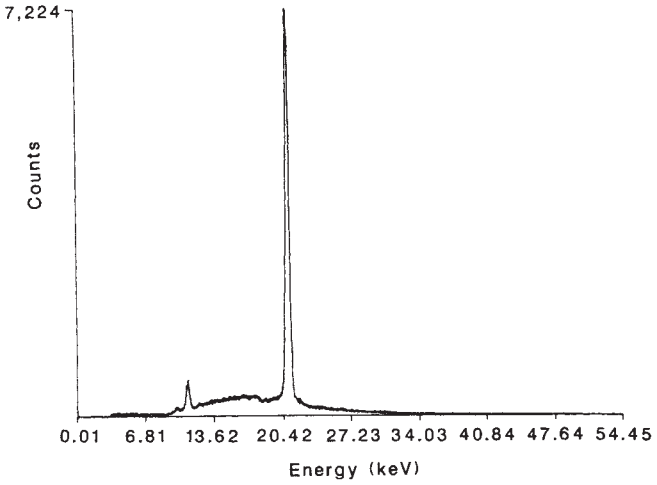

Fig. 1 Energy-dispersive X-ray diffraction pattern of H_2O-ice at 128 ± 2 GPa and 300 K. The sample, together with small chips of ruby for pressure determination, was confined in a 50-μm hole drilled into a 0.5-mm T-301 stainless steel gasket that has been preindented to 50 GPa (ref. 22). The incident X-ray beam from the synchrotron was collimated to a width of ~10 μm, and the diffracted X-ray beam was collected with a Si(Li) detector at a scattering angle $2\theta = 18.51 \pm 0.12°$, which was calibrated with CeO_2 powder at ambient pressure. The strong line (21.07 keV) is consistent with the (110) diffraction peak of the b.c.c. oxygen sublattice. The low-energy feature at 11.15 keV is an escape peak excited in the detector and does not correspond to a diffraction line. No background (Compton scattering from the anvils) has been subtracted. The measurements were performed at beamline X13A at the National Synchrotron Light Source (NSLS) at Brookhaven National Laboratory, New York.

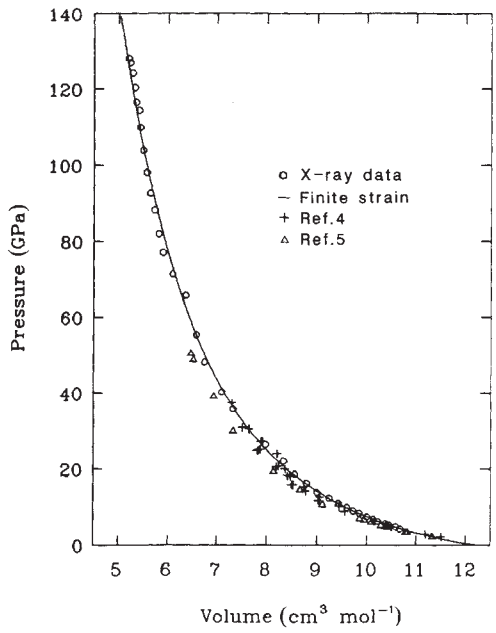

Fig. 2 Pressure–volume data and calculated room-temperature equation of state for H_2O-ice. The data of Munro *et al.*[4] have been corrected according to the nonlinear ruby-pressure scale of Mao *et al.*[20] The line represents a least-squares fit of the present data to a Birch–Murnaghan finite-strain equation of state, as developed for non-quenchable high-pressure phases by Jeanloz[23]. The equation of state is represented by the following parameters: the reference volume is the zero-pressure volume of ice I, $V_{01} = 19.66 \pm 0.06$ cm^3 mol^{-1}, and the best-fit zero-pressure volume of ice VII is $V_{02} = 12.3 \pm 0.3$ cm^3 mol^{-1}, with $V_{02}/V_{01} = 0.63$. The best-fit, zero-pressure bulk modulus and its pressure derivative for ice VII are $K_{02} = 23.7 \pm 0.9$ GPa and $K'_{02} = 4.15 \pm 0.07$.

and X-ray diffraction measurements at megabar pressures[22]. The diffraction pattern of ice VII was observed in this pressure range, consistent with previous work[4,5]. At lower pressures ice VII has a strong propensity to form single crystals in a diamond-anvil cell, as noted in earlier investigations[5]. With increasing pressure the crystals appeared to break up to give a polycrystalline sample over the diameter of the X-ray beam, although there was still evidence for preferred orientation of the crystals. From 4.3 to 66 GPa an X-ray beam diameter of 30 μm was used. With this beam size, the uncertainty in the pressure determined by ruby fluoresence increased with pressure above 20 GPa, as a result of increasing pressure gradients across the sample. The beam size was therefore reduced to ~10 μm at higher pressures (>70 GPa), and care was taken to measure the pressure from a small ruby grain embedded within the diffracting volume element of the ice. This significantly improved the precision of the ruby measurement at higher pressure. In addition, with a beam size of ~10 μm, there was no broadening of the diffraction pattern from pressure gradients. Figure 1 shows a representative energy-dispersive diffraction pattern at the highest pressure of our measurements. The strong line can be indexed as the (110) diffraction peak of the b.c.c. oxygen sublattice of the ice VII structure. Sometimes the (220) line, which is much weaker in the measured spectra, was also observed.

Figure 2 shows pressure–volume relations calculated from the diffraction pattern assuming a b.c.c. oxygen sublattice, and Table 1 lists the numerical results. Within the resolution of the data, a continuous shift of the pattern is observed, and the results are fitted to a third-order finite-strain equation of state[23]. The pressure–volume data from the earlier studies are also shown. Munro *et al.*[4] used the earlier (linear) ruby-pressure scale, which tends to under-estimate the pressure at higher pressure (for example, 3% low at 30 GPa). We have corrected their pressures using the nonlinear ruby-pressure scale, which is currently calibrated to 180 GPa (ref. 21). The present results are in excellent agreement with the corrected data of Munro *et al.*[4] in the region of their maximum pressures (20–36 GPa). At lower pressures some discrepancies between the two studies are observed; these differences may be due to orientation effects resulting from the formation of large single crystals in the sample. The pressures obtained by Liu[5] are appreciably lower at a given volume than both our results and those of Munro *et al.*[4], particularly at higher pressures. It is possible that these differences are due to the fact that a large sample and X-ray beam were used in the previous study, and the ruby grains may have been in lower-pressure regions within the sample[5].

Figure 3 compares the experimental equation of state determined from our data with the results of the theoretical models used in planetary studies. The Saltpeter and Zapolsky[11] curve shows the results of a Thomas–Fermi–Dirac (TDF) calculation with electron correlation in the region of the present measurements. This calculation significantly underestimates the density in the 100 GPa range. In each of the remaining calculations[12–15], a TDF approach was used in the limit of very high pressures (for example, 10^6 GPa). At low densities, experimental data (including temperature-reduced liquid-state data) were used to constrain the equation of state; various interpolation schemes between the two data sets were employed at intermediate pressures. Of these calculations, the equation of state obtained by Ree[12] agrees most closely with experiment (above 2.5 g cm^{-3}) and was specifically applied to the calculation of properties of fluid H_2O at high pressures. On the basis of TDF predictions for the low-temperature solid, Hubbard[2] has suggested that temperature-induced electronic excitations in fluid H_2O soften the equation of state under shock conditions. As our results are obtained at low temperatures relative to the shocked states (300 K compared with >3,000 K at high pressures), the extra

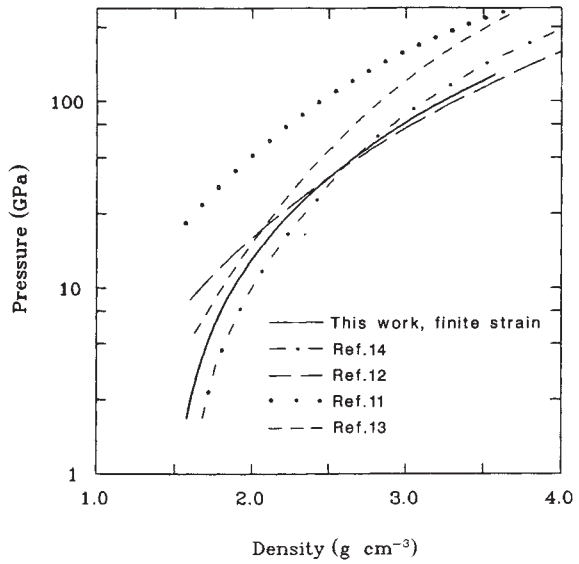

Fig. 3 Comparison of the experimental and theoretical equations of state for H_2O at high pressures and densities (see Hubbard[2], p. 61). The Saltpeter and Zapolsky[11] result represents the TDF limit for dense H_2O. The calculations of Ree[12], Reynolds and Summers[13], and Zharkov and Trubitsyn[14] are semi-empirical: the curves were determined by interpolation from low-pressure experimental data and the results of quantum statistical calculations at high pressures. The Ree[12] curve is a fit to his 0 K isotherm by Hubbard and MacFarlane[15]. All theoretical calculations are for $T = 0$ K.

Table 1 Pressure–volume data for H_2O-ice to 128 GPa at 300 K

P (GPa)	V_m (cm^3 mol^{-1})	P (GPa)	V_m (cm^3 mol^{-1})
4.3 ± 0.1	10.68 ± 0.03	40.3 ± 1.2*	7.11 ± 0.02
4.9 ± 0.1	10.59 ± 0.03	48.2 ± 1.5†	6.75 ± 0.02
5.4 ± 0.1	10.45 ± 0.03	55.4 ± 2.5†	6.58 ± 0.02
5.7 ± 0.1	10.38 ± 0.03	65.8 ± 2.5†	6.36 ± 0.02
6.3 ± 0.1	10.22 ± 0.03	71.4 ± 0.6‡	6.09 ± 0.02
6.7 ± 0.1	10.13 ± 0.03	77.0 ± 0.5	5.90 ± 0.02
7.5 ± 0.1	10.00 ± 0.03	82.0 ± 0.7	5.81 ± 0.02
8.4 ± 0.1	9.85 ± 0.03	88.0 ± 1.0	5.73 ± 0.02
9.0 ± 0.1	9.73 ± 0.03	92.5 ± 0.7	5.64 ± 0.01
9.9 ± 0.1	9.60 ± 0.03	98.0 ± 0.7	5.57 ± 0.01
11.0 ± 0.1	9.44 ± 0.03	104.0 ± 1.0	5.50 ± 0.01
12.3 ± 0.1	9.25 ± 0.03	110.0 ± 0.7	5.44 ± 0.01
13.8 ± 0.1	9.00 ± 0.02	113.5 ± 0.7	5.42 ± 0.01
16.2 ± 0.1	8.79 ± 0.02	116.0 ± 1.0	5.35 ± 0.01
18.6 ± 0.1	8.56 ± 0.02	120.0 ± 1.0	5.33 ± 0.01
22.1 ± 0.3*	8.34 ± 0.02	124.0 ± 1.0	5.28 ± 0.01
26.5 ± 0.5*	7.98 ± 0.02	127.0 ± 1.0	5.24 ± 0.01
36.0 ± 0.9*	7.33 ± 0.02	128.0 ± 2.0	5.20 ± 0.01

The errors listed for the pressures are those associated with the determination of the peak position of the ruby R_1 band, except where indicated, These errors arise from both peak broadening and instrumental effects. The principal contribution to the errors listed for the molar volumes is the standard error in the 2θ calibration for the energy-dispersive diffraction measurement.

* Magnitude of the quoted error is interpolated between that resulting from uncertainty in the R_1 position and that due to the pressure gradients measured above 48 GPa.

† Error is determined from the measured pressure gradient across the diameter of the X-ray beam.

‡ Smaller error follows from the reduction in beam size (see text).

softening of the equation of state, occurring in both fluid and solid H_2O, cannot be a thermal effect but must be due to errors in the application of the TDF model. Calculations for ice VII with semi-empirical intermolecular potentials developed for the low-pressure phases of H_2O also give a significantly less compressible equation of state at high pressure (>20 GPa) than is measured experimentally[24].

There have been two spectroscopic studies indicating that ice VII will transform to another phase at 40–50 GPa (refs 7, 8). These investigations, made at different temperatures (100 and 300 K), suggested that the high-pressure phase is that of symmetric ice X, which is characterized by hydrogens located at the midpoint between the oxygens on the body diagonal of the oxygen b.c.c. sublattice. Hirsch and Holzapfel[8] have observed a transition consistent with this structural change, which is first-order at 100 K and appears to involve a small volume change. Our results, obtained at 300 K, indicate that if such a transition occurs in this pressure range the transition must proceed either continuously or with a small volume change ($\lesssim 0.1$ cm^3 mol^{-1}). Some deviations in the measured pressure-volume data are apparent (for example, at 66 GPa), suggesting small discontinuities in the equation of state; however, these deviations are approximately equal to the uncertainty in the pressure. We have therefore fitted all of the data with a single equation-of-state function. It is likely that further spectroscopic measurements may provide a more sensitive probe of structural distortions of the oxygen lattice (as well as proton ordering[6–9]) than might be apparent in this study, considering the limited number of diffraction peaks observed, and the possibility that a small splitting of the peaks may not be resolved by the energy-dispersive diffraction technique.

On the basis of these results, however, it appears that larger (reconstructive) transformations involving the oxygen sublattice do not occur in ice compressed at room temperature to 128 GPa. Polian *et al.*[9] have suggested that ice may transform to a dense phase with the oxygens forming a face-centred cubic sublattice at ~100 GPa, but no such transition is observed here. In addition, pressure-induced amorphization does not occur on compression of ice VII, an effect that occurs in the open, low-density structures (at lower temperatures)[3]. Finally, we note that the ice samples in the present experiments remained transparent up to 128 GPa, with no sign of band-gap closure indicative of the metallic transition[9,25]: the ice band gap remains above the absorption edge of the diamond window of the high-pressure cell (~3 eV), as in solid H_2 under similar pressures[26]. This behaviour constrasts with that of solid O_2, in which pressure-induced electronic excitation at visible wavelengths in the 100 GPa range has been observed[27]. From the standpoint of planetary and satellite modelling, it is clear that H_2O-ice should be considered a transparent insulating material over the pressure-temperature range of this study. Previous reports of metallic conduction in compressed ice in the 100 GPa range may be a result of poorly characterized pressures or problems associated with the electrical measurements[25].

The authors are grateful to the following for support of this research: the National Synchrotron Light Source, Brookhaven National Laboratory, which is supported by US Department of Energy, NASA and the Carnegie Institution of Washington. D.E.C. acknowledges support from D.O.E. Division of Materials Sciences.

Received 22 June; accepted 29 September 1987.

1. Hobbs, P. V. *Ice Physics* (Clarendon, Oxford, 1974).
2. Hubbard, W. B. *Planetary Interiors* (Van Nostrand Reinhold, New York, 1984).
3. Mishima, O., Calvert, L. D. & Whalley, E. *Nature* **310**, 393–395 (1984).
4. Munro, R. G., Block, S., Mauer, F. A. & Piermarini, G. *J. appl. Phys.* **53**, 6174–6178 (1982).
5. Liu, L.-g. *Earth planet. Sci. Lett.* **61**, 359–364 (1982).
6. Walrafen, G. E. *et al. J. chem. Phys.* **77**, 2166–2174 (1982).
7. Polian, A. & Grimsditch, M. *Phys. Rev. Lett.* **52**, 1312–1314 (1984).
8. Hirsch, K. R. & Holzapfel, W. B. *J. chem. Phys.* **84**, 2771–2775 (1986).
9. Polian, A., Besson, J. M. & Grimsditch, M. in *Solid State Physics under Pressure* (ed. Minomura, S.) 93–98 (Terra Scientific, Tokyo, 1985).
10. Mitchell, A. C. & Nellis, W. J. *J. chem. Phys.* **76**, 6273–6281 (1982).
11. Saltpeter, E. E. & Zapolsky, H. S. *Phys. Rev.* **158**, 876–886 (1967).
12. Ree, F. Report UCRL-52190, Lawrence Livermore Lab., Livermore, California (1976).
13. Reynolds, R. T. & Summers, A. L. *J. geophys. Res.* **70**, 199–208 (1965).
14. Zharkov, V. N & Trubitsyn, V. P. *Physics of Planetary Interiors*, (Pachart, Tucson, Arizona, 1978).
15. Hubbard, W. B. & MacFarlane, J. J. *J. geophys. Res.* **85**, 225–234 (1980).
16. Baublitz, M. A., Arnold, V. & Ruoff, A. L. *Rev. scient. Instrum.* **52**, 1616–1624 (1981).
17. Jephcoat, A. P. *et al. Eos* **67**, 1216 (1986).

18. Zha, C. S. *et al. Eos* **67**, 1216 (1986).
19. Mao, H. K. *et al. Bull. Am. phys. Soc.* **32**, 798 (1987).
20. Mao, H. K., Bell, P. M., Shaner, J. W. & Steinberg, D. J. *J. appl. Phys.* **49**, 3276-3283 (1978).
21. Bell, P. M., Xu, J. & Mao, H. K. in *Shock Waves in Condensed Matter* (ed. Gupta, S.) 125-130 (Plenum, New York, 1986).
22. Jephcoat, A. P., Mao, H. K. & Bell, P. M. in *Hydrothermal Experimental Techniques* (eds Ulmer G. C. & Barnes, H. L.) Ch. 19 (Wiley, New York, 1987).
23. Jeanloz, R. *Geophys. Res. Lett.* **8**, 1219-1222 (1981).
24. Grimsditch, M., Rahman, A. & Polian, A. in *Materials Res. Soc. Symp.* Vol. 22 (eds Homan, C., MacCrone, R. K. & Whalley, E.) 143-146 (Elsevier, New York, 1984).
25. Liu, L.-g. & Bassett, W. A. *Elements, Oxides, Silicates - High-Pressure Phases with Implications for the Earth's Interior*, 92-94 (Oxford University Press, New York, 1986).
26. Mao, H. K., Bell, P. M. & Hemley, R. J. *Phys. Rev. Lett.* **55**, 99-102 (1985).
27. Desgreniers, S., Vohra, Y. & Ruoff, A. L. *Bull. Am. phys. Soc.* **32**, 762-763 (1987).

Internal waves and whitecaps

S. A. Thorpe, M. B. Belloul & A. J. Hall*

Department of Oceanography, The University, Southampton, SO9 5NH, UK
* Institute of Oceanographic Sciences, Deacon Laboratory, Wormley, Godalming, Surrey GU8 5UB, UK

There are numerous reports of internal waves being 'made visible' on the sea surface by their effect on the surface-wave field and the production of bands of steeper, often breaking, waves separated by zones of relatively calm water[1-5]. The effect is sometimes quite dramatic. There are accounts of a 'low roar' as the bands of breaking waves, 'walls of white water', pass a vessel[6]. The bands are sometimes visible from aircraft[7], on ships, radar[8,9] and are observed from satellites[10-15]. In the Bay of Biscay 'boils' have been reported on the sea surface in the calm zones, and appear to be related to pulses of nutrients from the thermocline[16]. The position of the roughest water has been commonly reported to be above the part of the internal wave in which the thermocline is most rapidly falling[3,5] (as sketched in Fig. 1) except in very light winds (< 3.5 m s^{-1}), when this appears generally to be the calmest zone[16]. There are, however, few simultaneous observations of surface and internal waves and none, to our knowledge, which has both quantified the frequency of the breaking waves and established their position relative to the internal waves. Here we have used an upward-pointing side-scan sonar to obtain a sub-surface view of bands of rough water and whitecaps on the sea surface associated with internal waves travelling on a pycnocline. The sonar provides a means to measure the surface currents induced by the internal waves, the position, or phase, of the surface-wave breaking relative to the internal waves, and to quantify the frequency of wave breaking. The effect of wave breaking caused by wave–current interaction is to transfer momentum from the surface waves to the currents, with a phase which tends to diminish the internal waves in the cases studied. The enhanced turbulence caused by wave breaking may be effective in mixing or eroding the pycnocline.

Explanations of these phenomena rely on the surface currents produced by internal waves. In light winds such currents concentrate surface-active films in the region above internal-wave troughs, leading to a reduction in capillary ripples and to bands of calm water[17]. In the more common, windy, conditions, the interactions of surface waves and the currents appear to amplify long surface waves where the current opposing them is greatest[15]. Shorter waves are most amplified where the horizontal gradient of the current reaches a (negative) minimum. We consider here one part of this wave–current interaction, the part which results in breaking waves and their consequent effect on internal waves and the thermocline.

Observations have been made using a two-beam side-scan sonar (248 kHz, 0.08-ms pulse length) mounted on a tripod resting on the sea bed at a depth of ~35 m near Oban on the west coast of Scotland[18] (Fig. 1). The beams lie in two vertical planes at right angles to each other and are ~1 m wide at the sea surface. The overlying water is stratified by the tidal discharge of brackish water from a nearby sea-loch, Loch Etive.

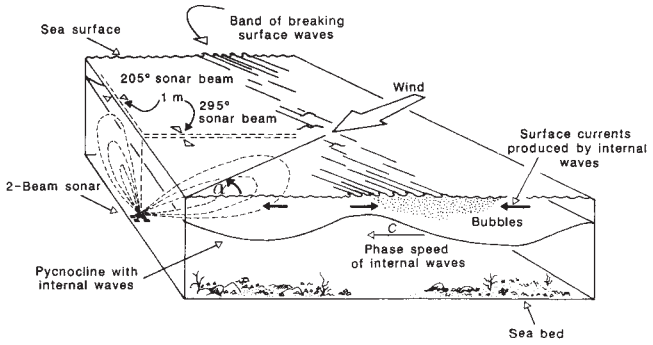

Fig. 1 Sketch showing internal waves producing near-surface currents, shown by arrows, which modulate the wind-generated surface waves to produce bands of rough water and whitecaps or breaking waves. The bottom-mounted sonar has two vertical beams at right angles.

Packets of internal waves are produced when the front heading this discharging density current is reflected from the coast ~2 km from the sonar position, and these are visible on the surface[19]. Figure 2 shows three sonograph records of these waves made apparent through the motion they produce in the sound-scattering, sub-surface clouds of bubbles created by breaking surface waves. These breaking waves usually occur in groups. Because the phase speed of the waves exceeds the group speed, successive waves approach the centre of the group, break, leave a cloud of bubbles, and then continue to advance relative to the group but with diminishing amplitude[20]. The pattern of successive breaking waves leaves 'dashed lines' on the sonograph, indicating regions where the specular reflection from the convoluted air-water interface in the breaking waves is large (for example, at A, Fig. 2*a*, *b*), with 'plumes', that is, the bubble clouds (for example, B, Fig. 2*a*), being carried in the direction of the surface current. The speed, c_g, and direction of the group velocity of the surface waves are estimated from the slope of the dashed lines in two sonar beams. Using the dispersion relation, the speed provides an estimate of the wave period, $T_s = c_g/4\pi g$, where g is the acceleration due to gravity. The wave period may be determined independently from the undulating image of the surface immediately above the sonar.

The bubble plumes are advected by the surface currents produced by the wind, tide and, in these particular examples, by internal waves. The component of the current in the direction of the sonar beam is measured from the observed change in the range of the bubble clouds with time. Figure 2 shows variations in current with periods of ~5-10 min and wavelength, determined from components measured in the two sonar directions, of ~50-150 m, which are due to internal waves[18]. The propagation speed and direction of the waves, and the fluctuations in surface current, may all be determined from the sonograph. The fluctuations are approximately periodic about the mean current preceding the waves. This is more consistent with their approximating to a regular wave train (as sketched in Fig. 1) than to a sequence of solitary waves with unidirectional pulses of current as observed, for example, in the Sulu Sea[5].

We have analysed the available records to determine the properties, and relative propagation directions, of the surface and internal waves and the distribution of breaking waves (see Table 1). The frequency of breaking is greatly enhanced in some regions of the internal waves, leading to the darker bands of sound reflectors (the bubble clouds), in Fig. 2. Breaking is most frequent in those regions of the internal waves where the fluctuating current tends to oppose the propagation direction of the surface waves (see also ref. 15), being typically twice as frequent there as in the zones of minimum wave breaking (the ratio r, Table 1). (The averaging over one-quarter wave periods tends to reduce the value of r, but the number of examples available